Incorporating K-RDT Product into SAS Deep Convection Scheme for Improved Short-term Prediction of Heavy Rainfall in South Korea

Namgu Yeo[1], Eun-Chul Chang[1,2], and Ki-Hong Min[3]

[1]Department of Atmospheric Science, Kongju National University, Gongju, Republic of Korea.

[2]Earth Environment Research Center, Kongju National University, Gongju, Republic of Korea.

[3]Department of Astronomy and Atmospheric Sciences, Kyungpook National University, Daegu, Republic of Korea.

Corresponding author: Eun-Chul Chang (echang@kongju.ac.kr)

Key Points:

- This study utilizes the Korea Rapid Developing Thunderstorms product in predicting heavy rainfall events.
- A simple nudging technique was applied to the deep convection scheme to incorporate the convective cell information.
- The results showed that small-scale cell information has a crucial impact on heavy rainfall prediction.

Abstract

In this study, we examined the potential of the Korea Rapid-Development Thunderstorm (K-RDT) product obtained from a geostationary meteorological satellite to improve the short-term prediction of heavy rainfall caused by a mesoscale convective system over South Korea. Specifically, we utilized a simple nudging technique to integrate K-RDT data into the Simplified Arakawa Schubert (SAS) deep convection scheme of the Global/Regional Integrated Model System (GRIMs) Regional Model program (RMP). Our analysis focuses on selected cases of heavy rainfall. The nudging experiments outperformed the control experiments in terms of precipitation forecasts. Notably, the experiment that used longer nudging times produced the best results. Our results also demonstrate that the K-RDT, with its resolution of 1 km, can detect small-scale convective cells that have clear impacts on large-scale atmospheric fields. This suggests that incorporating such small-scale information into numerical weather prediction (NWP) models can significantly improve forecasting skill, especially when the model cannot represent subgrid-scale convection.

Plain Language Summary

In this study, we investigated how to improve short-term forecasts of heavy rainfall caused by mesoscale convective systems in South Korea. We used data from a geostationary meteorological satellite to identify small-scale convective cells, which can have a big impact on large-scale atmospheric fields. We then incorporated this information into a numerical weather prediction model using a simple nudging technique. Our results showed that the nudging experiments with longer nudging times produced the best precipitation forecasts compared to control experiments. This suggests that incorporating small-scale information into numerical weather prediction models can significantly improve forecasting skill, especially when the model cannot represent subgrid-scale convections. These findings have important implications for improving weather forecasting accuracy and preparedness for extreme weather events, which can have significant impacts on public safety and infrastructure.

1 Introduction

Over 50% of total precipitation in Northeast Asia occurs during the East Asian summer monsoon season. In South Korea, summer rainfall has significantly increased over the last century (1913–2012), with a higher increase in instances and the intensity of extreme rainfall than in total precipitation (Baek et al., 2017; Jung et al., 2011). Heavy rainfall generally occurs over the Korean Peninsula during warm seasons in association with typhoons, synoptic disturbances, and convective systems (Lee et al., 1998). Understanding the rapidly developing convective systems is crucial, as they not only develop rapidly and strongly but also have impacts on society and the economy.

Lee and Kim (2007) classified heavy precipitation systems (HPSs) during summer (June-July-August; JJA) from 2000 to 2006 over the Korean Peninsula into four types based on their scale, shape, and movement: isolated thunderstorms (ISs), convection bands (CBs), squall lines (SLs), and cloud clusters (CCs). Among the four types, ISs are the smallest and develop in an isolated manner, with widths generally smaller than a few tens of kilometers. CBs and SLs are similar in that they develop linearly and have smaller widths compared to their lengths. However, they differ in terms of their movement and structure. CCs are the most frequent type and consist of a meso-β scale of convective precipitation embedded in a continuous area of stratiform rainfall. Jo et al. (2019) also classified localized heavy rainfall events during the warm season (June-July-August-September; JJAS) from 2005 to 2017 in South Korea into three groups based on clustering precipitation patterns. While these studies did not investigte the detailed mechanisms of convective systems, they demonstrated that convective systems exhibit different characteristics such as temporal and spatial scale, intensity, and variability.

Convective systems are generally caused by strong updrafts resulting from thermal instability induced by inhomogeneous radiative heating near the surface. Usually, these systems have spatial and temporal scales of several tens to hundreds of kilometers and several hours, respectively. Still up-to-date operating numerical weather prediction (NWP) models struggle to predict heavy precipitation systems. These forecast failures occur when the models either fail to predict the convective system or underestimate the precipitation intensity, even when the rainfall spatial distributions are well captured. The numerical model can underestimate rainfall intensity when the spatial resolution is insufficient to depict the small-scale convective systems. Therefore, accurately predicting covnective systems with NWP models remains challenging.

Continuous efforts have been made to improve simulations of heavy rainfall events using NWP models (Korsholm et al., 2015; Qie et al., 2014; Fierro et al., 2014; Dixon et al., 2016; Segele et al., 2013). Previous studies employed cloud-resolving models that generally had a grid spacing of less than 4 km and did not require a convective parameterization scheme. However, although high-resolution models may explicitly resolve convection, they are not fully represented at that resolution, which is a gray zone issue (Hong and Dudhia, 2012). In addition, global NWP models operate at a coarser resolution, with the Global Forecast System (GFS) of the National Centers for Environmental Prediction (NCEP), the Global Data Assimilation and Prediction System (GDAPS) of the Korea Meteorological Administration (KMA), and the Integrated Forecasting System (IFS) of the European Center for Medium-Range Weather Forecasts (ECMWF) having a horizontal resolutions of approximately 10 km. Therefore, using a convective parameterization scheme in NWP models is essential to accurately predicting heavy rainfall events.

There are many meteorological satellite products, including the Rapid-Development Thunderstorm (RDT) product, which was initially developed for nowcasting thunderstorms in Météo-France and the Nowcasting Satellite Application Facility. Lee et al. (2020) have presented a novel RDT technique for use in Korea (K-RDT). K-RDT provides information on the developing stages of convective clouds: growing, mature, or decaying. In this study, the stage information from the K-RDT product was nudged into the simplified Arakawa-Schubert (SAS) convection scheme to improve the predictability of convective systems in South Korea. In addition, its impact on real-world simulations was analyzed in terms of short-term forecasts. Section 2 presents an overview of two selected heavy rainfall cases. In Section 3, the K-RDT product-nudging technique and experimental setup are described. The results and conclusions are presented in Sections 4 and 5.

2 Case Overview

The goal of this study is to evaluate the impact of the nuding technique on heavy rainfall forecasts. Two cases were selected: heavy rainfall occurring locally due to convective systems in South Korea. Fig. 1 shows the radar rain rates for both cases. The first case (Case 1) was a heavy rainfall event that occurred in Cheongju, located at 127.511°E and 36.584°N, on July 16, 2017. The rainfall intensity reached a record-breaking 86.2 mm h^{-1} for 0700–0800 LST July 16, 2017, with a 1-day total rainfall amount of 290.2 mm in the city. In Case 1, convective system was organized over the Yellow Sea at 0000 LST on July 16, 2017 (Fig. 1a). The convective system, moving southeastward inland, gradually developed and leds to heavy rainfall in the middle part of the Korean Peninsula at 0400 LST (Fig. 1b). At 0800 LST, the precipitation system is located near Cheongju. New convective systems continued to develop and grow in this region for approximately 4 h from 0700 LST to 1100 LST in July 2017 (Fig. 1c). This led to unprecedented heavy rainfall in Cheongju. The second case (Case 2: August 24, 2017) is a heavy rainfall event over the northern and western parts of South Korea (Fig. 1d-f). In this case, precipitation occurred as a narrow rain band with a width of 100 km, which elongated in a southwest-northeast direction and moved southward. As noted by Lee and Kim (2007), the squall line moves southeastward in a direction perpendicular to the rainband. In addition, as the squall line moved, the rain band became narrower and more organized up to 1600 LST on Augsut 24, resulting in intensified precipitation over the middle of the Korean Peninsula.

Fig. 2 shows 1-day accumulated precipitation for each case obtained from the KMA Automatic Weather Station (AWS) observations and the forecast results from the Local Data Assimilation and Prediction System (LDAPS), which is the operational regional high-resolution forecast model of the KMA with a grid spacing of 1.5 km. In Case 1, the precipitation was distributed in the central and northern parts of South Korea (Fig. 2a), with a rainfall core over Cheongju. The simulated rainfall core in the LDAPS shifted northward from Cheongju, and the amount of precipitation in the core was underestimated compared with the AWS observations (Fig. 2c). The LDAPS simulated a heavily emphasized rainband shape for observation. In Case 2, the observed rainfall core was located in the mid-eastern part of the Korean Peninsula. The LDAPS simulated a narrower line-shaped rainband than the AWS observations. In addition, the simulated LDAPS precipitation was underestimated over the southern part and shifted eastward in the middle of South Korea (approximately 36°N–37°N).

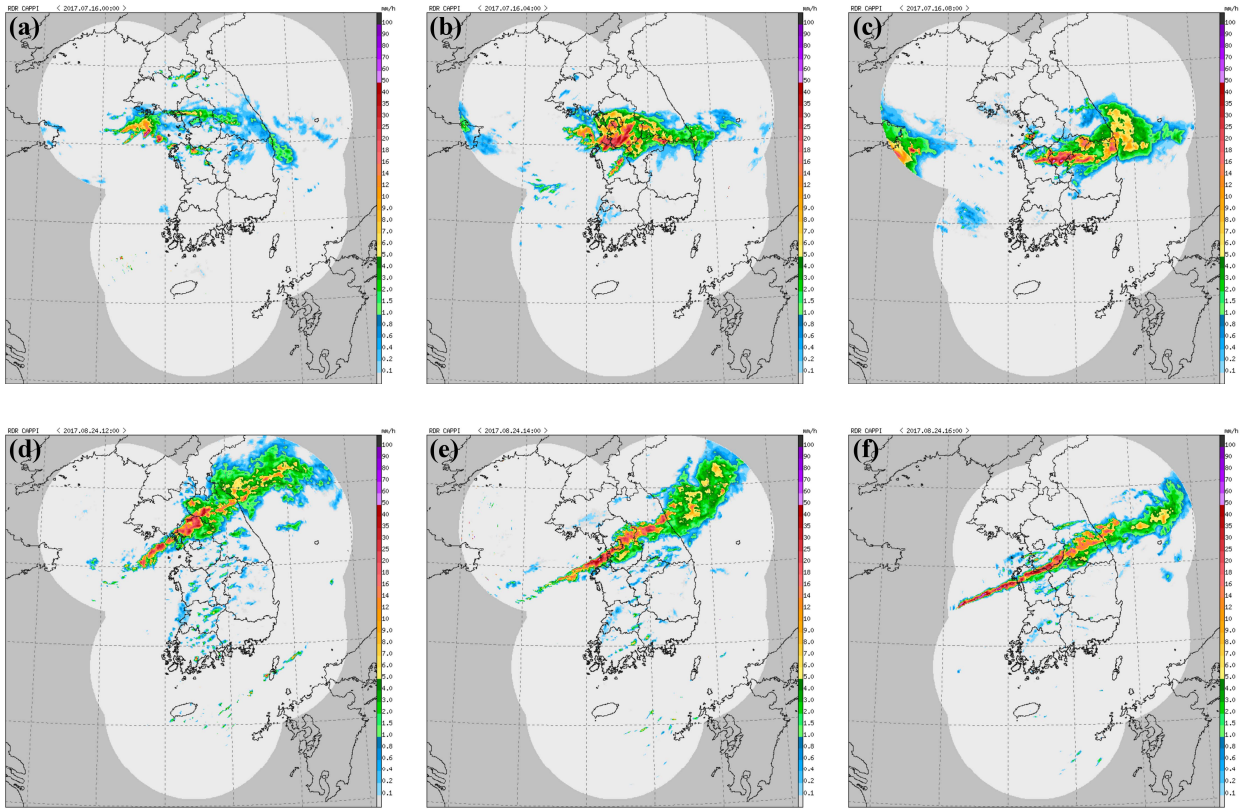

Figure 1. CAPPI 1.5 km radar imagery for (a) 0000 LST, (b) 0400 LST and (c) 0800 LST on July 16, 2017. (d), (e), and (f) show imagery for 1200 LST, 1400 LST and 1600 LST on August 24, 2017, respectively.

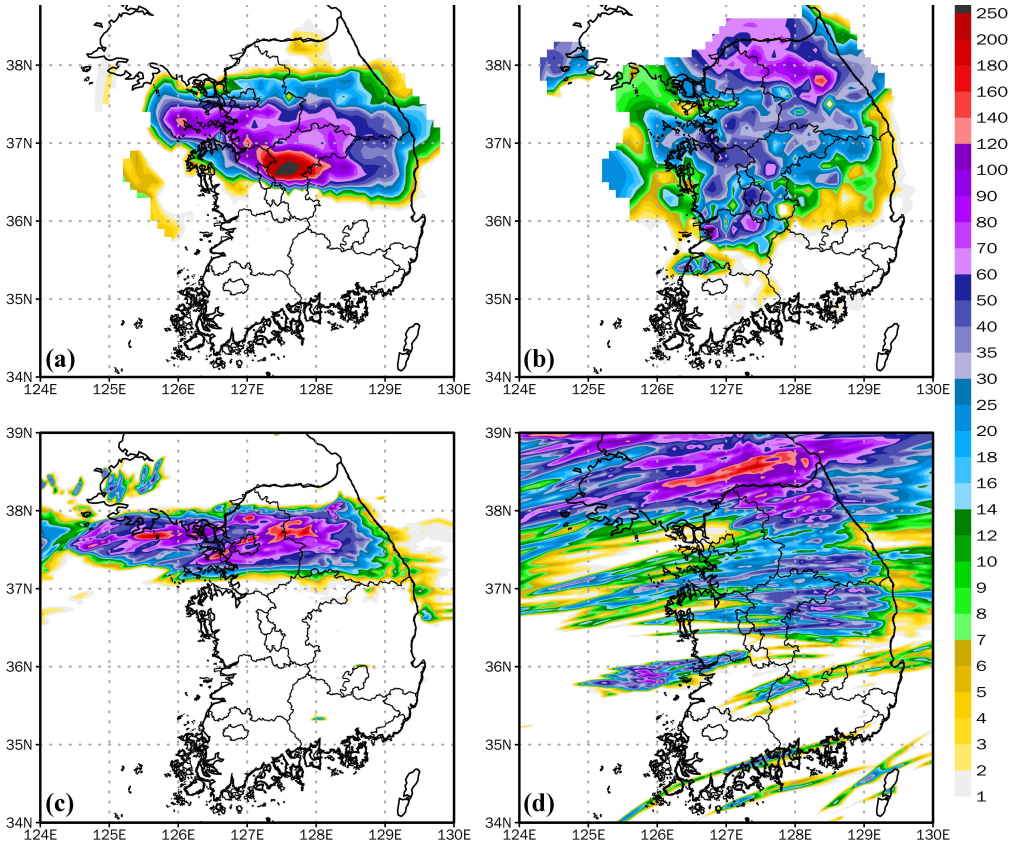

Figure 2. 1-day accumulated precipitation (mm) from AWS observations and LDAPS. Left column shows the precipitation on July 16, 2017 obtained from (a) AWS observations and (c) LDAPS forecast field initiated at 1500 LST on July 15, 2017 and right column presents the precipitation on August 24, 2017 obtained from (b) AWS observations and (d) LDAPS initiated at 2100 LST on August 23, 2017.

Fig. 3 presents the simulated precipitation from LDAPS at each time point during the rainfall evolution, which is shown in Fig. 1. In Case 1, LDAPS successfully simulated the precipitation system near the Gyeonggi Bay, but failed to capture the rainfall over the inland region as shown in the radar imagery at 0000 LST on July 16, 2017. As the system moved inland, the rainfall core appeared to shift slightly northward, far from Cheongju. Additionally, heavy rainfall in the LDAPS occurred predominantly in the maritime region, which contrasts with the rain rate depicted in the radar imagery at 0400 LST on July 16, 2017. Over time, the LDAPS predicted a greater northward shift in rainfall compared to radar imagery at 0800 LST on July 16, 2017. For Case 2, LDAPS predicted the distribution of rainfall in a band formation at 1200 LST on August 24, 2017. As the band system moved southward, the overall distribution of precipitation was found to be similar to that depicted in the radar imagery, exhibiting an elongated shape stretching from the southwest to the northeast at 1400 LST on August 24, 2017. Over time, the LDAPS failed to produce a narrow, organized squall line, which was evident in the radar imagery at 1600 LST on August 24, 2017.

Fig. 4 shows the K-RDT product from the HIMAWARI-8 satellite. For Case 1, it is shown that the convective cells of the mature stage were in the middle region of South Korea, including Cheongju City, where the LDAPS failed to accurately simulate the precipitation system and heavy

rainfall was detected (Fig. 4b). Furthermore, new convective systems in the growing stage were also detected by the K-RDT algorithm in the vicinity of Cheongju City, where the LDAPS failed to produce any precipitation (Fig. 4c). The convective cells detected by the K-RDT algorithm have the potential to contribute to precipitation that is not produced by LDAPS. For Case 2, the K-RDT algorithm provides information about the band shape structure of convective cells, whereas the LDAPS presents band structures that are disconnected (Fig. 4e-f). K-RDT algorithms can detect numerous clouds, partly due to the input of CI information. However, the K-RDT algorithm was effective in identifying convective clouds that generated heavy rainfall in Cheongju City and contributed to the formation of narrow and elongated squall lines. Thus, integrating the K-RDT products, which indicate the developmental stage of convective clouds, into the cumulus parameterization scheme of NWP models may lead to improvements in the accuracy of the prediction of heavy rainfall.

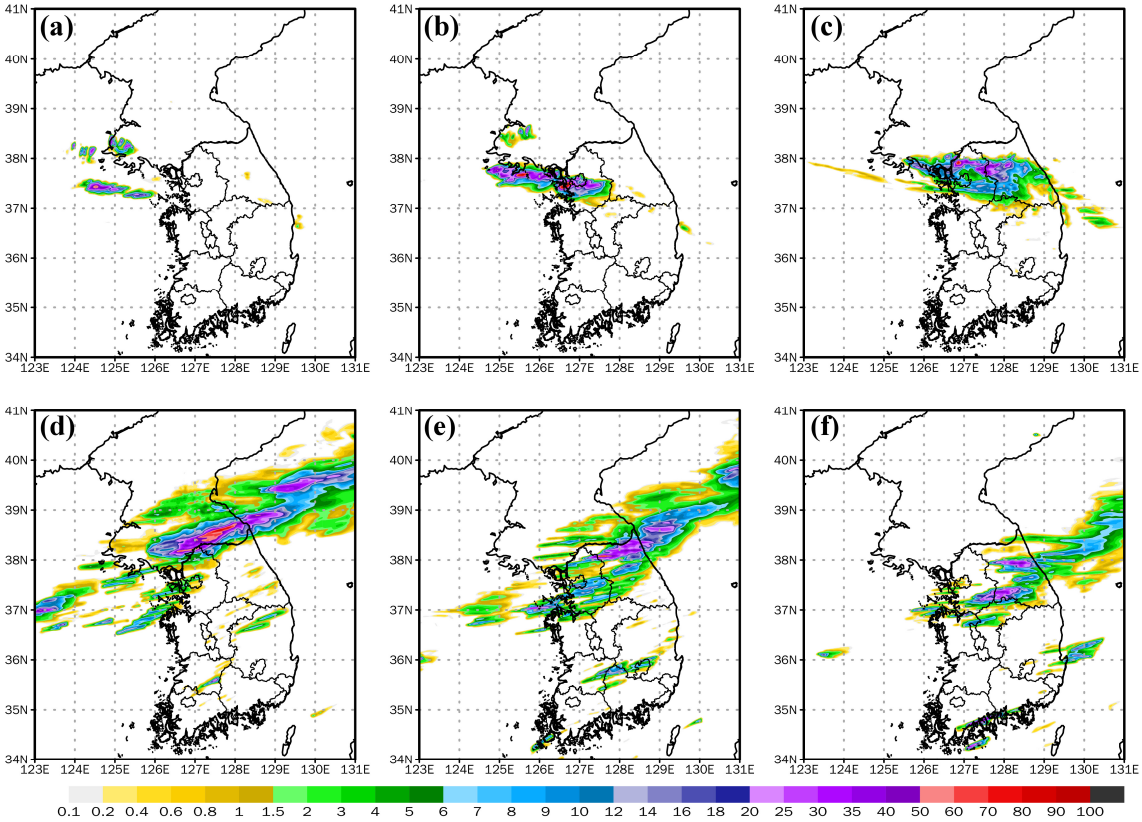

Figure 3. Same as in Fig. 1 except for the LDAPS forecast field of precipitation (mm h^{-1}). Left and right columns show forecasts from 0000 LST on July 16, 2017 and 1200 LST on August 24, 2017, respectively.

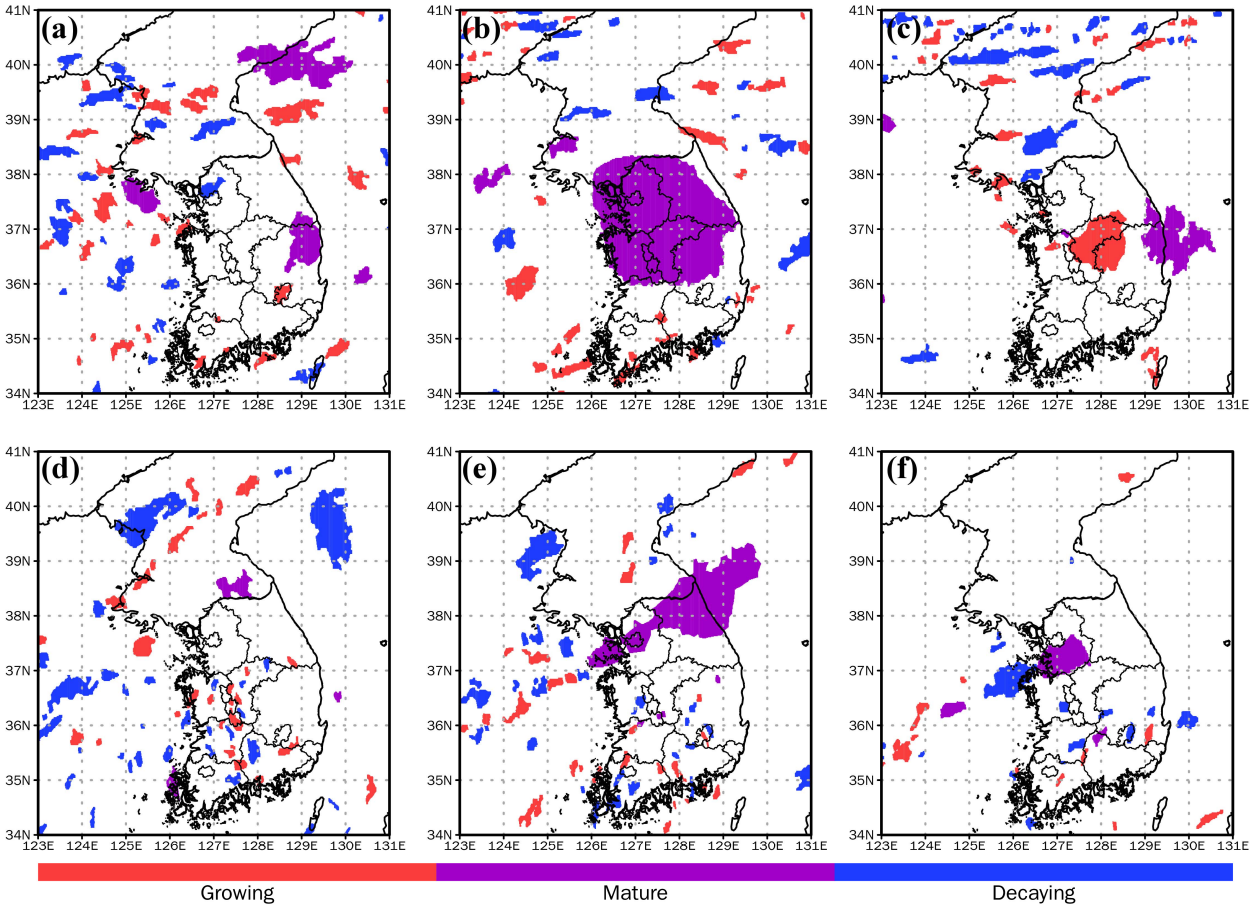

Figure 4. Same as in Fig. 1 except for K-RDT product. Each color indicates a development stage of convective clouds.

3 Materials and Methods

3.1 K-RDT Data Nudging process

In this study, the K-RDT product which includes small-scale features of convective clouds was nudged into the SAS deep convection scheme. The K-RDT product was retrieved from the HIMAWARI-8 satellite, which performs similarly to the 2nd Geostationary Earth Orbit Korea Multi-Purpose Satellite (GEO-KOMPSAT-2A, GK-2A) in South Korea. Despite being launched in December 2018, GK2A was not used for the K-RDT algorithm, as a proxy collected by the HIMAWARI-8 satellite was utilized due to its similar channel characteristics. Lee et al. (2020) presented a newly developed RDT technique for Korea (K-RDT), in which CI data were paired with a modified RDT algorithm for the GK2A. The K-RDT algorithm will be continuously improved using the GK2A data. The SAS scheme employed in this study applies a mass-flux type to adjust the environmental fields and has been continuously modified (Hong and Pan, 1998; Han and Pan, 2006; Byun and Hong, 2007; Han and Pan, 2011). It was first implemented in the National

Centers for Environmental Prediction (NCEP) Medium-Range Forecast model in 1993 (Pan and Wu, 1995) and has since been continuously developed. The cloud-base mass flux is obtained using a quasi-equilibrium assumption, where the destabilization caused by the large-scale atmosphere is balanced by the stabilization of the cumulus. The parameterization closure is determined based on the large-scale and cumulus cloud work functions.

The number of K-RDT grids within one model grid is approximately 100 because the grid spacings of the model and K-RDT product used in the study are 10 km and 1 km, respectively. To represent one developmental stage on the model grid using 100 K-RDT grid points, the following method is used: First, the K-RDT grid points are counted within 5 km of the model, which consists of 100 K-RDT grids. The most-counted K-RDT represents the developmental stage of the convective cloud in the model grid. For instance, as shown in Fig. 5, the number of each K-RDT stage is counted as in the growing, mature, and decaying stages, respectively. In this case, the model grid is considered to be in a mature stage. The development stage defined in the model grid provides information for the nudging process. When the development stage is determined at the model grid, the nudging process, which is revised from previous methods (Rogers et al., 2000; Lagouvardos et al., 2013; Giannaros et al., 2016) is initiated. There are three methods of nudging for different conditions when the K-RDT product is converted on the model grids:

1) Suppress convection at the grid point where the K-RDT stage does not exist, but the convection is calculated in the SAS deep convection scheme; 2) modify the mass flux where the convective cloud is detected in K-RDT and convection is also activated in the model by the convection scheme; and 3) force convection where the thunderstorm is present but the model convection scheme does not produce it. For the condition in method 1 the updraft speed at the cloud base decreases reasonably enough for the air parcel to not exceed the level of free convection (LFC). For condition 2), where the K-RDT stage exists and convection is also activated in the SAS scheme, the cloud-base mass flux, which is calculated in the SAS scheme itself, is modified according to the K-RDT stage. The maximum threshold of mass flux in the SAS scheme is determined as a $g\Delta p/\Delta t$ (Han and Pan, 2011), where Δp is the model layer depth at the cloud base, g and Δt are gravity and the model time step, respectively. If the grid indicates a growing stage, the final mass flux is determined as the mean value between the original mass flux calculated using the SAS scheme and the maximum threshold. The maturity and decay grids are modified as the maximum threshold and original mass flux, respectively. The process for condition 3 consists of two steps. The first step involves verifying whether convection is activated in the SAS scheme before proceeding with the convection. If the convection is not initiated, the upward motion is forcibly increased in the air parcel to overcome convective inhibition (CIN). Subsequently, the cloud depth of the triggered grid is checked because the SAS scheme requires a pressure difference between the cloud base and the top of the cloud to identify whether there is a deep convective cloud. If the pressure difference is higher than 150 hPa, the cloud-base mass flux is modified according to the K-RDT stage, as in condition 2. However, if the pressure difference is less than the threshold, the grid column is forced by adding moisture by 0.1 g kg^{-1} to prevent sudden convection disappearance of the K-RDT cell when the nudging process ends. This process is

iterated up to a maximum of 10 times when the added moisture reaches 1 g kg^{-1}. A flowchart of the nudging process is shown in Fig. 6.

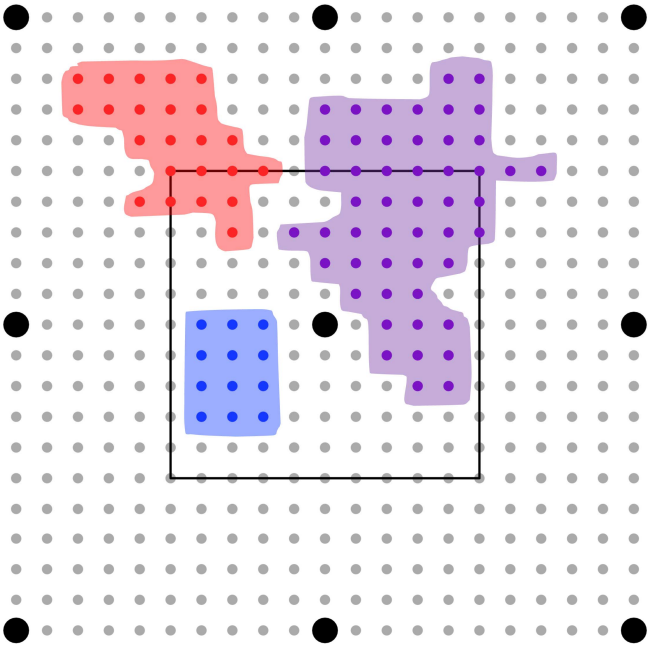

Figure 5. Schematic for the method to convert the K-RDT grid into the model grid. Big black dots indicate model grids, and small gray dots are K-RDT grids. The red, violet, and blue dots present the growing, mature, and decaying stages of the K-RDT, respectively.

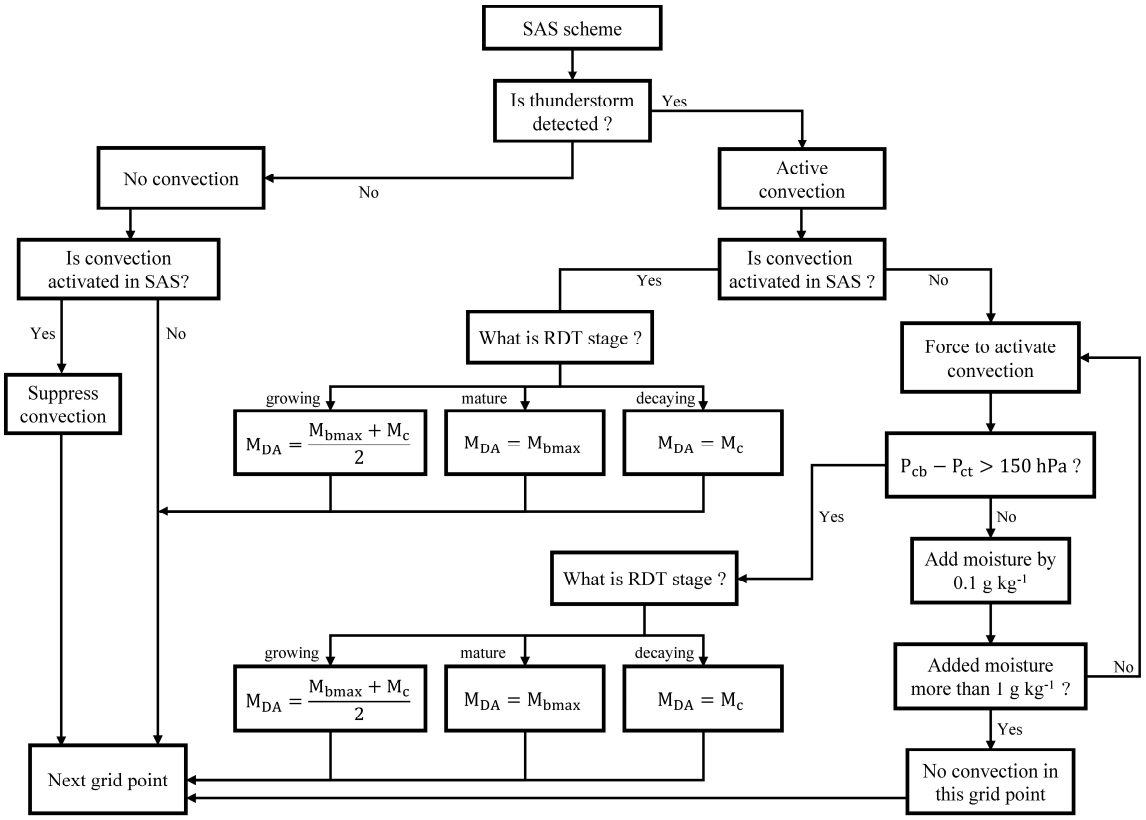

Figure 6. Flow chart of the decision processes for convection in each grid point during the nudging period.

3.2 Model and experimental setup

The regional model used in this study is the Global/Regional Integrated Model system (GRIMs) regional model program (RMP) with a two-dimensional perturbation method (Hong et al., 2013). The model uses physics parameterization schemes that include: the long wave scheme (Chou et al., 1999), the short wave scheme (Chou and Suarez, 1999), the weather research and forecasting single-moment 5-class microphysics scheme (Hong et al., 2004), the SAS deep convection scheme (Han and pan, 2011), the GRIMs shallow convection scheme (Hong et al., 2012), the cloudiness scheme (Hong et al., 1998), the Yonsei University boundary layer scheme (Hong et al., 2006) with enhanced stable boundary layer mixing (Hong, 2010), the Noah land surface model (Chen and Dudhia, 2001), the ocean mixed layer model (Kim and Hong, 2010), the convective and orographic gravity wave drag parameterization schemes (Chun and Baik, 1998), and (Kim and Arakawa, 1995). The domain consists of 300×281 grids with Lambert conformal conic projection and a horizontal resolution of 10 km (Fig. 7), which has a grid spacing similar to that of a global operating NWP model, such as GFS, GDAPS, and IFS. Δt for model integration is 60 s, and 42 sigma vertical layers are used. The 6-hourly ECMWF's ERA-interim reanalysis data (Dee et al., 2011) is used as the initial and lateral boundary conditions. A control experiment and two subsequent K-RDT nudging experiments are performed for each heavy rainfall case to identify the impact of K-RDT nudging on the mesoscale convective system simulation. Fig. 8 summarizes

the experiments performed in this study. For Case 1, the control (C1CNTL) and two nudging experiments (C1KN08 and C1KN12) are simulated from 1500 LST on July 15, 2017, to 0300 LST on July 17, 2017. The C1CNTL experiment is conducted without K-RDT nudging, whereas the C1KN08 and C1KN12 experiments involve K-RDT nudging for 8 h and 12 h from the initial time, respectively. Following this period, model simulations are performed without nudging. The K-RDT is nudged every 10 min, which corresponds to the temporal resolution of the K-RDT product. The analysis of Case 1 focuses on the period from the end of the nudging period to 8 h thereafter in the C1KN12 experiment, which has the longest nudging period among all the nudging experiments. For Case 2, C2CNTL and two nudging experiments (C2KN12 and C2KN16) are also performed from 2100 LST on August 23, 2017, to 0900 LST on August 25, 2017. C2KN12 and C2KN16 are subjected to the nudging process for 12 h and 16 h, respectively, from the initial time. The scope of analysis pertaining to Case 2 is the period commencing from the termination of nudging and continuing for an additional 9 h in the C2KN16 experiment, characterized by the longest nudging period.

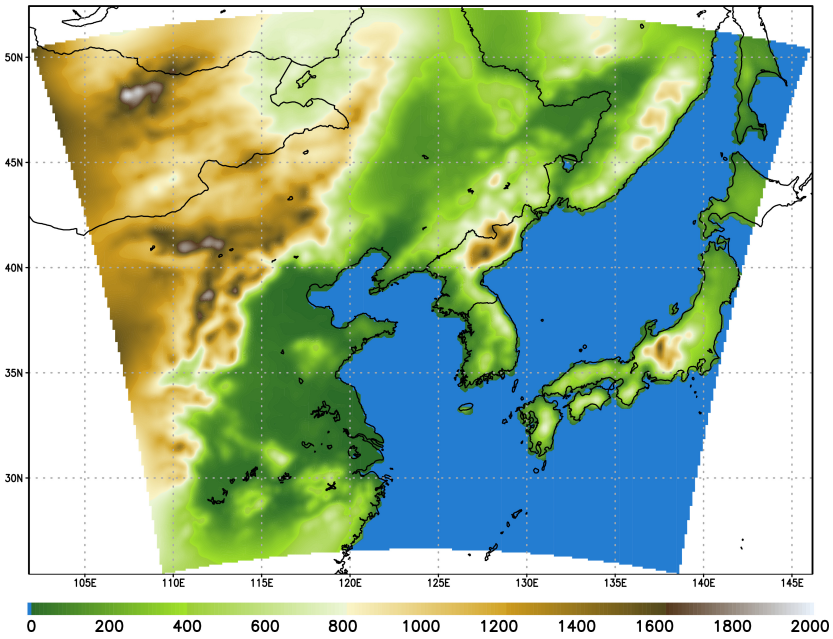

Figure 7. Model domain. Terrain heights (m) are shaded.

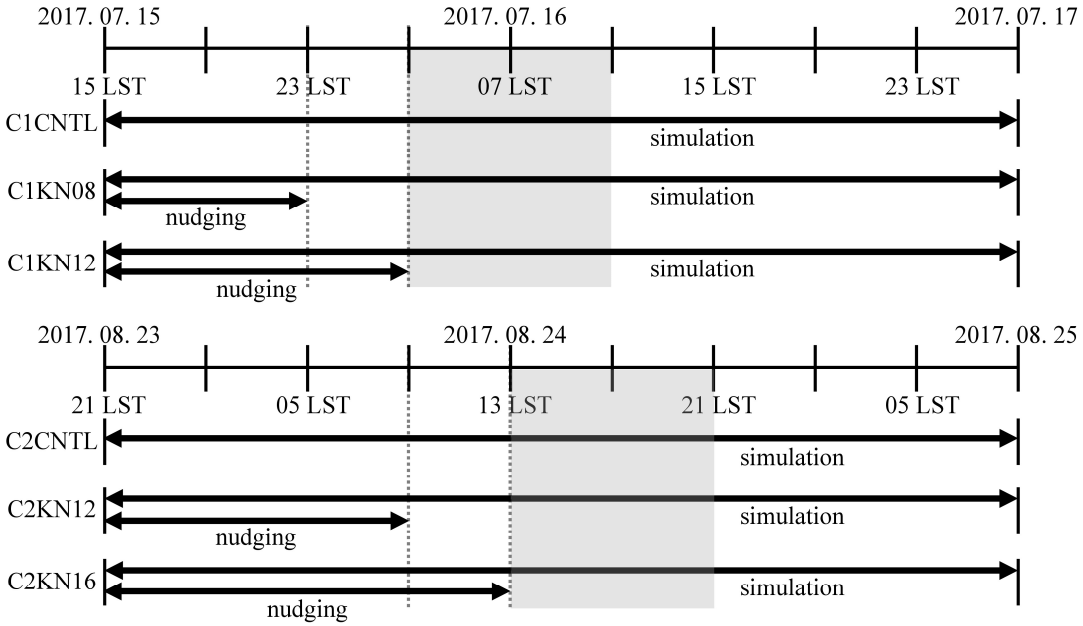

Figure 8. Summary of the experiments performed in this study. Shaded area is analysis period.

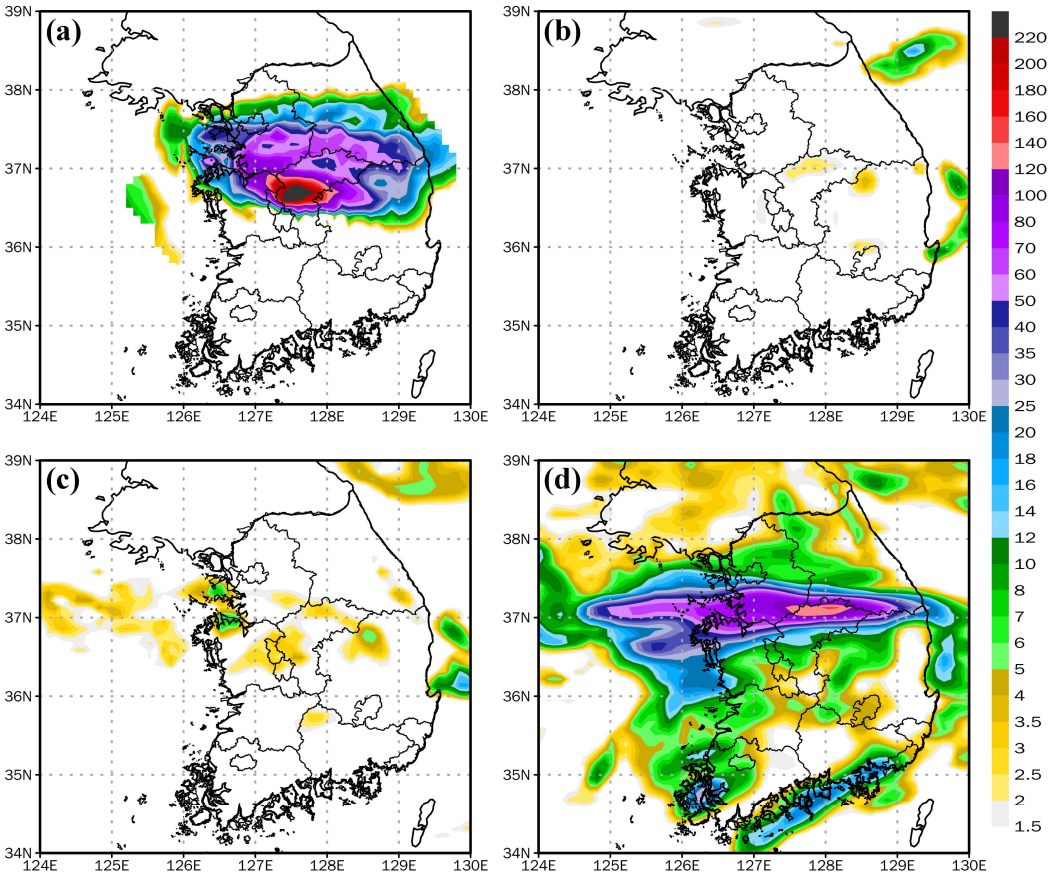

Figure 9. 8-h accumulated precipitation (mm) at 1100 LST on July 16, 2017 from (a) AWS observations, (b) C1CNTL, (c) C1KN08, and (d) C1KN12 experiments.

4 Results

4.1 Precipitation simulations

Fig. 9 presents the 8-h accumulated precipitation from 0300 LST on July 16, 2017 to 1100 LST on the same day, obtained from AWS observations as well as from the C1CNTL, C1KN08, and C1KN12 runs over South Korea. The accumulated period, highlighted by shaded areas in Fig. 8, covers a localized heavy rainfall event that occurred in Cheongju City from the time when nudging ends in C1KN12. The C1CTNL experiment fails to capture the heavy rainfall system over South Korea, although it do capture some light precipitation of approximately 3 mm near Cheongju City (Fig. 9b). On the other hand, C1KN08 simulates a larger amount of precipitation than C1CNTL in Cheongju City, but there is still a significant difference compared to the AWS (Fig. 9c). The C1KN12 experiment also disagrees in that the precipitation core location is shifted northeastward and the maximum rainfall amount is underestimated compared to the observation. However, the overall performance of the C1KN12 simulation is better than that of the other experiments. C1KN12 simulates the core near Cheongju City and localized heavy rainfall in the central part of Korea, as shown in AWS. The enhanced precipitation of C1KN12 results from nudged convective cells detected by the K-RDT algorithm.

The convective cells in the vicinity of these regions are mostly detected by the K-RDT algorithm after 2300 LST on July 15, 2017 (Fig. 4a-c). These cells are applied to the C1KN12, but not to C1KN08, because the nudging process of C1KN08 is inactivated at 1500 LST on July 15, 2017. Consequently, the performance of the model is enhanced when the K-RDT is nudged for a relatively longer time, including short-living convective cells, because the cell information rapidly disappears after the nudging ends. Fig. 10 shows the 9-h accumulated precipitation from 1300 LST on August 24, 2017, to 2200 LST on August 24, 2017 obtained from AWS observations, Tropical Rainfall Measuring Mission (TRMM) Multisatellite Precipitation Analysis (TMPA), and the experiments. The accumulated period is shown as the shaded area in Fig. 8. In this rainfall case, TMPA data is used due to limitations in the coverage of the AWS data over the maritime region. The analysis period is from the time when the nudging ends in C2KN16 to the time when heavy precipitation by the squall line occurred over Korea. C2CNTL fails to capture the precipitation core in the northeastern region of South Korea, specifically near 128.5°E and 38°N, where a complex mountainous terrain is present. This is in contrast to the TMPA, which indicates values exceeding 80 mm in this area. Furthermore, C2CNTL fails to simulate other cores in the vicinity of 127.5°E and 38.5°N, which results in significantly lower levels of rainfall than the TMPA. In addition, C2CNTL produces large amounts of precipitation at 125.5°E and 37.5°N, north of Gyeonggi Bay. However, in the nudging experiments (C2KN12 and C2KN16), the amount of rainfall increases not only in the northeastern part of the complex mountainous terrain but also near 127.5°E and 38.5°N. These precipitation scores are clearly identified in C2KN16 and are attributed to K-RDT nudging. We have found that K-RDT nudging can enhance the precipitation simulation by increasing the underestimated precipitation through the addition of missing convection information and decreasing the overestimated precipitation through the convection-suppressing process.

The improved results of the precipitation simulations are indicated through qualitative analysis and quantitative statistical scores. Table 1 presents the skill scores for the accumulated precipitation for each experiment compared with the AWS observations. The simulated

precipitation in each experiment is bilinearly interpolated to the AWS station points to calculate scores. The skill scores quantitatively indicate that the predictability of precipitation improves. In Case 1, the bias, RMSE, and spatial pattern correlation (PC) coefficients indicate that the prediction skills of the two nudging experiments (C1KN08 and C1KN12) are better than those of the C1CNTL run. In particular, the scores demonstrate noticeably improved results in the C1KN12 simulation. Similarly, in the second case, although the bias of the C2CNTL experiment is better than that of the C2KN12 experiment, the RMSE and PC of the nudging experiments (C2KN12 and C2KN16) are better than those of the C2CNTL experiment. C2KN16 exhibits the best performance.

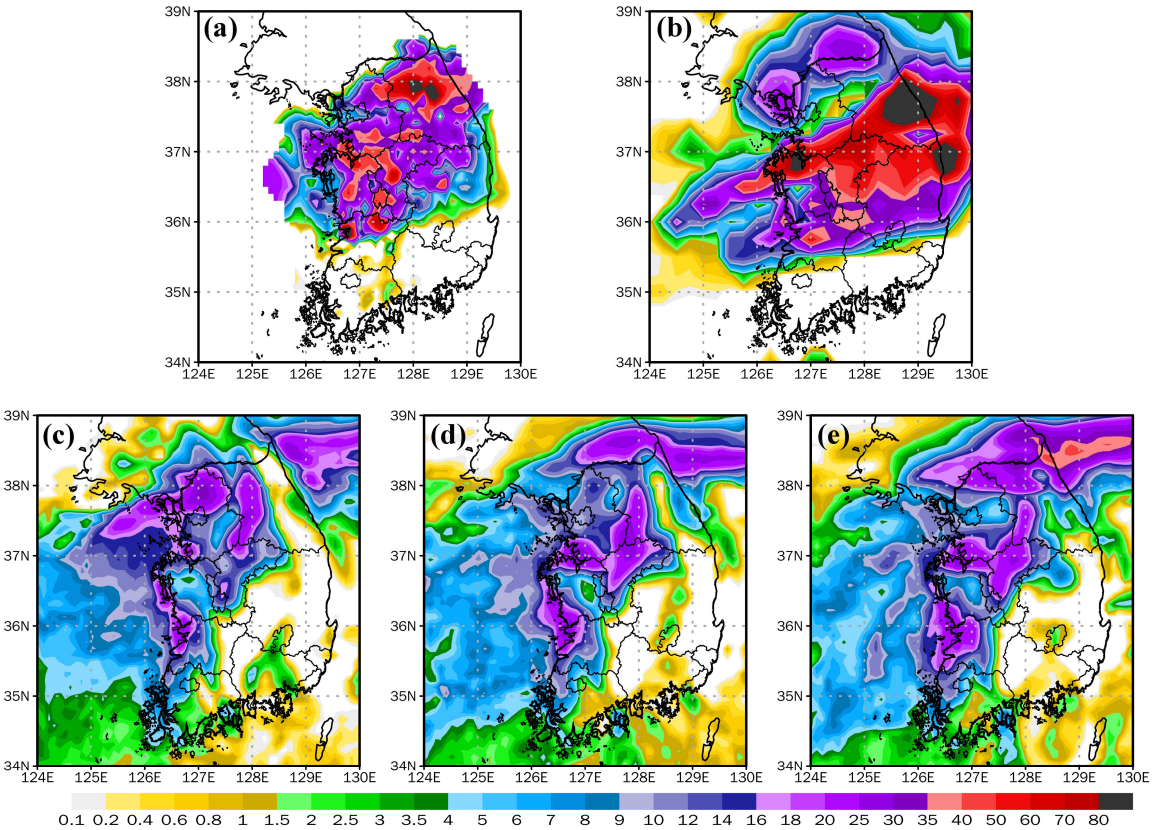

Figure 10. 9-h accumulated precipitation (mm) from 1300 to 2200 LST on August 24, 2017 for (a) AWS observations, (b) TMPA, (c) C2CNTL, (d) C2KN12, and (e) C2KN16 experiments.

Table 1. Verification statistics of accumulated precipitation with AWS observations. The period is the same as in Fig. 9 and 10. Bold indicates best performance among experiments.

EXP.	Bias	RMSE	PC
C1CNTL	–19.63	40.82	0.25
C1KN08	–19.33	40.43	0.43
C1KN12	**–3.27**	**32.19**	**0.50**
C2CNTL	–6.31	18.52	0.33
C2KN12	–6.80	17.59	0.47
C2KN16	**–5.64**	**16.94**	**0.49**

4.2 Impact of the K-RDT nudging on environment fields

Fig. 11 depicts the developmental stage of the K-RDT, mass flux, specific humidity, and temperature related to the CPS at 0250 LST on July 16, 2017, 10 min before the termination of nudging in the C1KN12 experiment. This is approximately 5 h before record-breaking rainfall occurred in Cheongju City. The mass flux is a crucial factor in determining the strength of convection, and the vertical profiles of specific humidity and temperature indicate thermal instability. These vertical profiles show the differences between the adjusted fields resulting from nudging in the SAS scheme and the fields prior to convection adjustment. In the SAS scheme, there are two main effects of cloud-base mass flux on the environmental fields: the warming effect resulting from the release of latent heat flux and the drying effect resulting from a decrease in atmospheric water vapor. It is demonstrated that a large cloud-base mass flux exists where the developing stage of convective cloud information is represented by the K-RDT at the model grid point (Figs. 11b and 11c). Moreover, the cloud-base mass flux is larger at the grid point of the growing stage than at the decaying stage. In particular, the mass flux is largest at the mature stage, indicating that convection occurs most strongly at this stage compared to the growing and decaying stages. The vertical temperature profile shows a warming effect caused by convective activity, and the specific humidity profile shows a moistening effect rather than a drying effect. Because specific humidity can be increased up to 1 g kg^{-1} in the nudging process, much moisture is sustained in the atmosphere, which may significantly affect the microphysical processes of the clouds in the microphysics scheme.

To analyze the impact of K-RDT nudging on atmospheric fields, we focus on the results of a heavy rainfall event in Cheongju City. The C1CNTL and C1KN12 results are compared with LDAPS data. Fig. 12 shows the low-level wind, geopotential height, and precipitable water at 0900 LST on July 16, 2017. This is the result 6 h after the end of the nudging process in the C1KN12 experiment. In the C1CNTL run, above the southern Yellow Sea, a prevailing southwesterly wind shitfts to a westerly direction near 37°N. The wind speed gradually increases, reaching a maximum in the eastern part of the Korean Peninsula. However, a significant change in the wind patterns is observed with K-RDT nudging, resulting in a dramatic increase in wind speed in the southern region of 37°N and a decrease in the northern region compared to the C1CNTL results (Fig. 12c). In addition, cyclonic flow is intensified in central South Korea with K-RDT nudging. These wind patterns are induced by a low system (Fig. 12e). The local low is a result of the K-RDT nudging process. Furthermore, the amount of precipitable water in South Korea is higher in the K-RDT nuding experiment than in C1CNTL. The results show that the small convective cells resolved at a 1 km resolution in the K-RDT product have important roles in changing meso- to synoptic-scale fields. Thus, heavy rainfall is attributed to the formation of a local low and increased availability of moisture due to the presence of small convective cells resolved at 1 km resolution in the K-RDT product, which have important roles in modifying meso- to synoptic-scale fields.

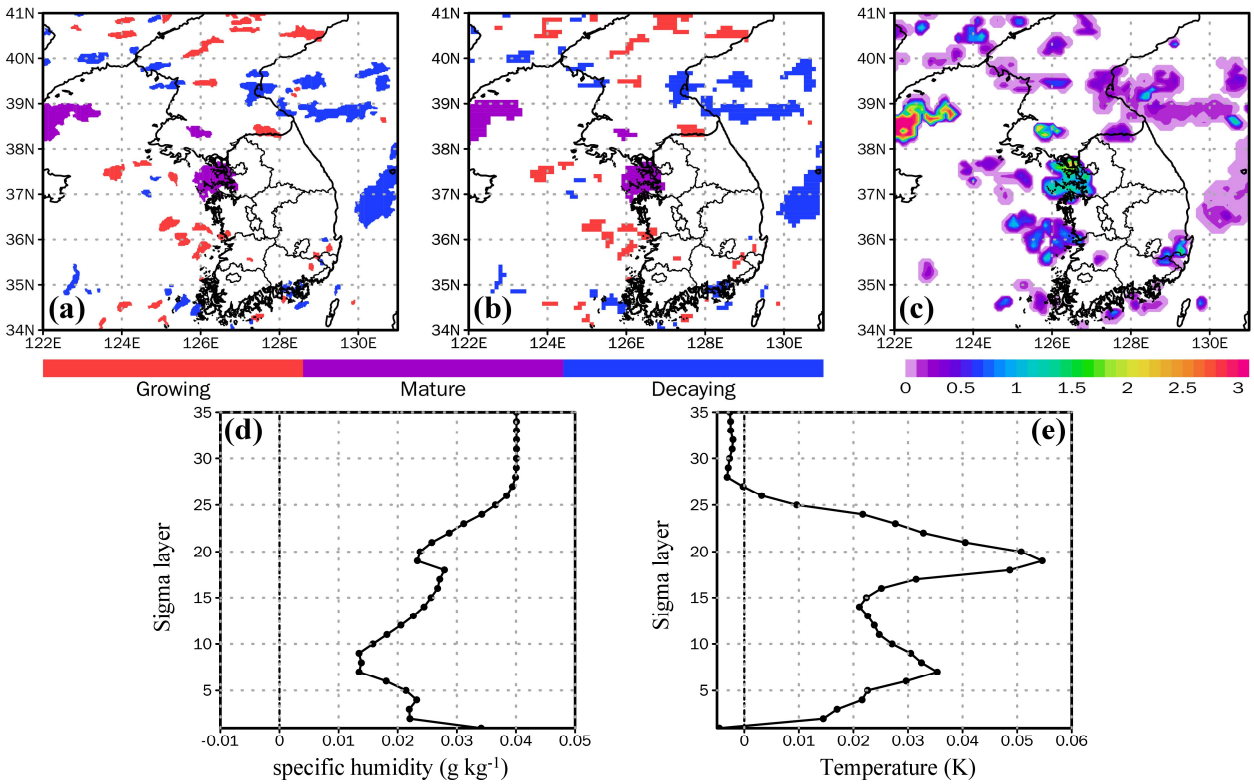

Figure 11. An example of K-RDT nudging process at 0250 LST on July 16, 2017 in the C1KN12 experiment. (a) and (b) are developing stages of convective cloud represented in the K-RDT grid and model grid, respectively. Red, violet, and blue indicate growing, mature, and decaying stages. (c) is a cloud-base mass flux (kg m^{-2} s^{-1}) calculated in the SAS scheme. (d) shows, in the model layer, the vertical profile of specific humidity (g kg^{-1}) difference between adjust field by convection and before to adjust field, the difference is averaged over 122°E–131°E and 34°N–41 °N. (e) is the same in (d) except for temperature (K).

Fig. 13 displays the vertical profile of the area-averaged moist static energy at 0900 LST on July 16, 2017, in each experiment, and the LDAPS. Heavy rainfall occurs in this area, and the results show an increase in moist static energy at most levels above 900 hPa, relative to C1CNTL. The addition of up to 1 g kg^{-1} specific humidity in the nudging process results in increased thermal instability, thereby enhancing upward motion. Dynamically, when a strong upward motion occurs, the air parcel converges at a lower level to conserve mass. In this rainfall event, the wind speed in the southern region of the strong upward motion area increases, while in the northern region, it decreases, with the prevalence of southwesterly and westerly. Wind direction and speed vary to achieve strong convergence. In the northern region, the westerly wind turns northerly, and the wind speed decreases, while in the southern region, westerly winds turn to southwesterly winds, and the wind speed increases to intensify convergence. Furthermore, the increased specific humidity in the atmosphere results in a large amount of precipitable water. Consequently, nudging the K-RDT product improves the predictability of the mesoscale convective system by incorporating small-scale features of convective clouds into the CPS scheme. Moreover, the existence of a great deal of precipitable water in the atmosphere and strong local upward motion

cause heavy rainfall in the narrow region. Therefore, representing a convective cell that is sufficient to generate large-scale atmospheric fields in the model grid is essential for forecasting heavy rainfall systems.

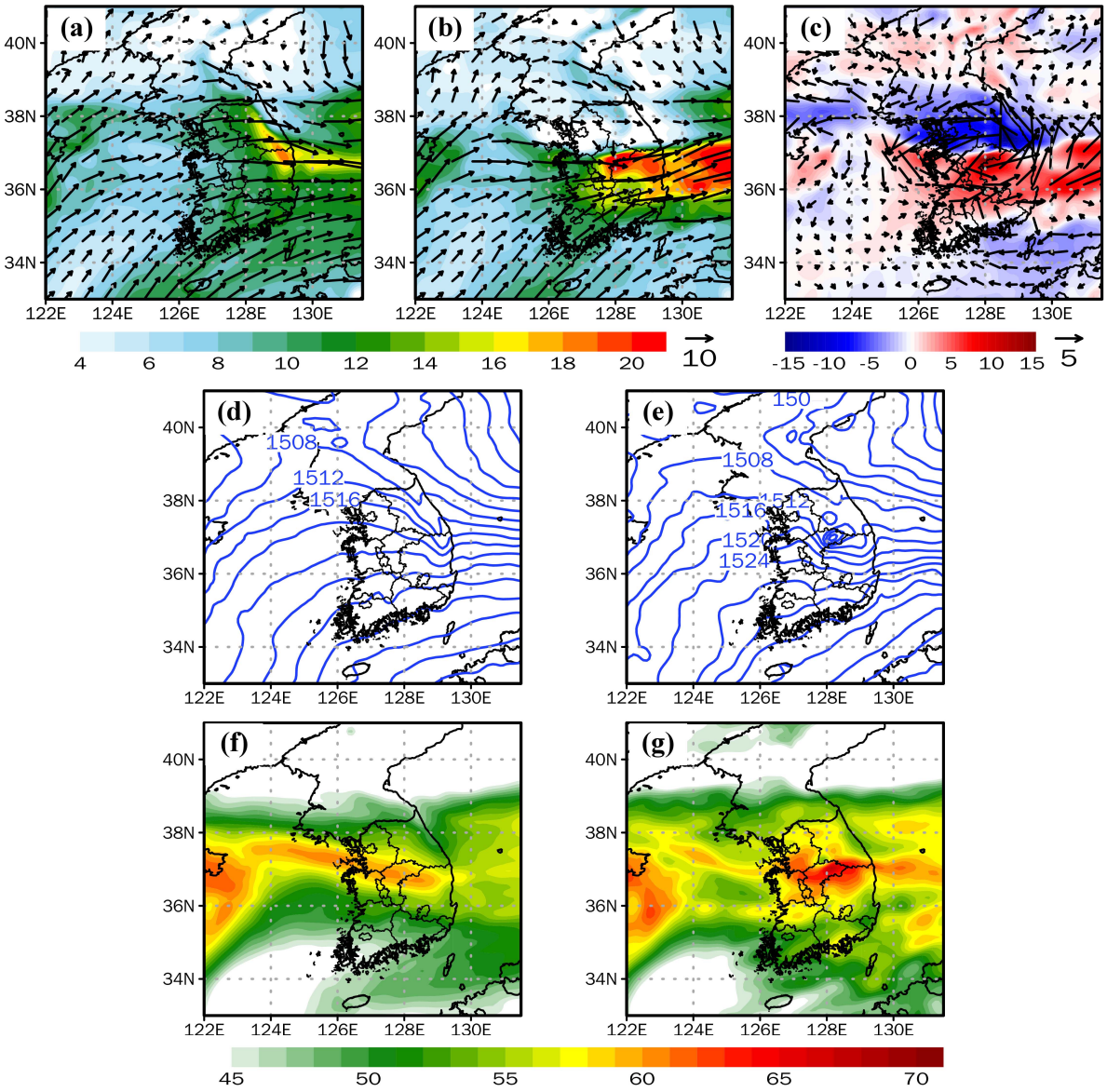

Figure 12. Atmospheric fields at 0900 LST on July 16, 2017 in the experiments. (a) and (b) show wind speed (shaded, m s^{-1}) and vector at 850 hPa level in the C1CNTL and C1KN12 experiment, respectively, (c) is the difference between C1KN12 and C1CNTL. (d) and (e) present geopotential height (gpm) at 850 hPa in the C1CNTL and C1KN12, respectively. (f) and (g) are the same as in (d) and (e) except for precipitable water (mm).

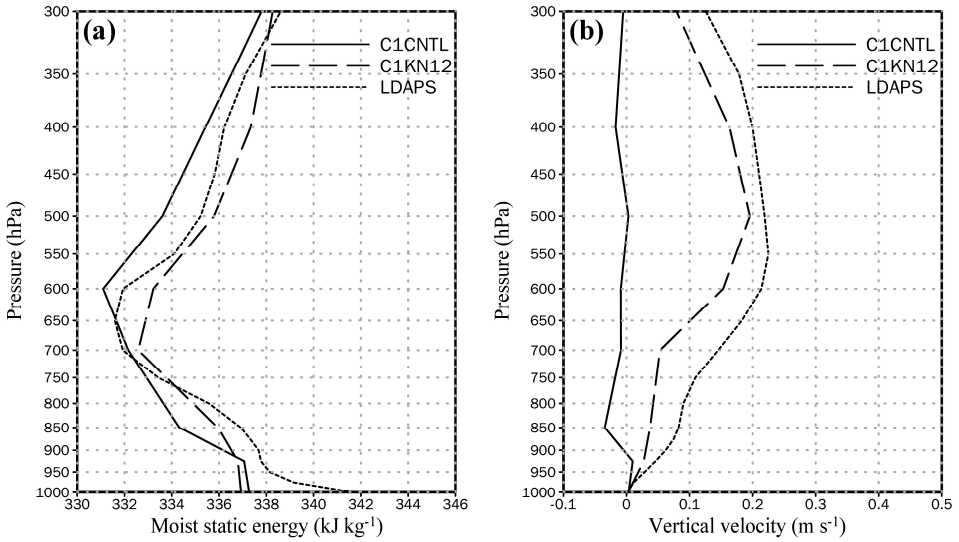

Figure 13. Vertical profile of (a) moist static energy (kJ kg^{-1}) and (b) vertical velocity (m s^{-1}) averaged over 127.5°E–129.0°E and 36.5°N–37.5°N at 0900 LST on July 16, 2017 in the C1CNTL, C1KN12, and LDAPS, respectively. The initial field of LDAPS is plotted.

5 Conclusions

This study aims to improve the prediction skill for heavy rainfall by nudging the K-RDT product, which indicates the developmental stage of convective clouds (i.e., growing, mature, and decaying) into the SAS deep convection scheme. Two heavy rainfall cases are selected: one involving localized heavy rainfall, and the other involving rainfall from a narrow squall line over South Korea. Simple nudging techniques are applied to each case, including the control (C1CNTL and C2CNTL) and two subsequent nudging experiments (C1KN08, C1KN12, C2KN12, and C2KN16). The results show that the precipitation prediction performance in the nudging experiments is better than that in the experiments without nudging, although the accuracy of the K-RDT product significantly influences the effectiveness of the nudging technique. Additionally, experiments with longer nudging periods show improved performance compared to those with shorter periods. This improvement is attributed to the increased specific humidity resulting from the nudging process, which affects the cloud microphysical processes in the microphysics scheme. Moreover, the increased moist static energy drives thermal instability, leading to strong upward motion and heavy rainfall caused by increased column precipitable water and strong vertical velocity. Therefore, the results suggest that the nudging technique used in the experiment is reasonable for improving the prediction skill of heavy precipitation in short-term forecasts despite its dependence on the spatial distribution of convective cell information detected by the K-RDT algorithm. Moreover, small-scale convective cells detected by the K-RDT with a 1-km resolution have a clear impact on meso- to synoptic-scale atmospheric fields, highlighting the importance of utilizing small-scale information on convective systems in NWP to improve the forecast skill in model systems that cannot accurately represent sub-grid scale convections.

Acknowledgements

This work was funded by the Korea Meteorological Administration Research and Development Program ‘‘Enhancement of Convergence Technology of Analysis and Forecast on Severe Weather’’ under Grant KMA2018-00121. This work was also supported by the research project of Kongju National University.

Data Availability Statement

The Global/Regional Integrated Model (GRIMs) Regional Model Program (RMP) is available at svn://210.106.80.229. The ERA-Interim data can be downloaded at https://apps.ecmwf.int/datasets/data/interim-full-daily/levtype=pl/. The Local Data Assimilation and Prediction System (LDAPS) forecast and Automatic Weather Station (AWS) of the Korea Meteorological Administration (KMA) are available at the Open MET Data Portal (https://data.kma.go.kr/cmmn/main.do).

References

Baek, H. J., Kim, M. K., & Kwon, W. T. (2017). Observed short-and long-term changes in summer precipitation over South Korea and their links to large-scale circulation anomalies. *International Journal of Climatology*, *37*(2), 972–986.

Byun, Y. H., & Hong, S. Y. (2007). Improvements in the subgrid-scale representation of moist convection in a cumulus parameterization scheme: The single-column test and its impact on seasonal prediction. *Monthly Weather Review*, *135*(6), 2135–2154.

Chen, F., & Dudhia, J. (2001). Coupling an advanced land surface–hydrology model with the Penn State–NCAR MM5 modeling system. Part I: Model implementation and sensitivity. *Monthly Weather Review*, *129*(4), 569–585.

Chou, M. D., & Suarez, M. J. (1999). *A solar radiation parameterization for atmospheric studies* (No. NASA/TM-1999-104606/VOL15).

Chou, M. D., Lee, K. T., Tsay, S. C., & Fu, Q. (1999). Parameterization for cloud longwave scattering for use in atmospheric models. *Journal of Climate*, *12*(1), 159–169.

491 Chun, H. Y., & Baik, J. J. (1998). Momentum flux by thermally induced internal gravity waves
492 and its approximation for large-scale models. *Journal of the Atmospheric Sciences*, *55*(21), 3299–
493 3310.
494 Dee, D. P., Uppala, S. M., Simmons, A. J., Berrisford, P., Poli, P., Kobayashi, S., Andrae, U.,
495 Balmaseda, M. A., Balsamo, G., Bauer, P., Bechtold, P., Beljaars, A. C. M., van de Berg, L.,
496 Bidlot, J., Bormann, N., Delsol, C., Dragani, R., Fuentes, M., Geer, A. J., Haimberger, L., Healy,
497 S. B., Hersbach, H., Hólm, E. V., Isaksen, L., Kållberg, P., Köhler, M., Matricardi, M., McNally,
498 A. P., Monge-Sanz, B. M., Morcrette, J.-J., Park, B.-K., Peubey, C., de Rosnay, P., Tavolato, C.,
499 Thépaut, J.-N., & Vitart, F. (2011). The ERA-Interim reanalysis: Configuration and performance
500 of the data assimilation system. *Quarterly Journal of the Royal Meteorological Society, 137*(656),
501 553–597.
502 Dixon, K., Mass, C. F., Hakim, G. J., & Holzworth, R. H. (2016). The impact of lightning data
503 assimilation on deterministic and ensemble forecasts of convective events. *Journal of Atmospheric*
504 *and Oceanic Technology*, *33*(9), 1801–1823.
505 Fierro, A. O., Gao, J., Ziegler, C. L., Mansell, E. R., MacGorman, D. R., & Dembek, S. R. (2014).
506 Evaluation of a cloud-scale lightning data assimilation technique and a 3DVAR method for the
507 analysis and short-term forecast of the 29 June 2012 derecho event. *Monthly Weather Review*,
508 *142*(1), 183–202.
509 Giannaros, T. M., Kotroni, V., & Lagouvardos, K. (2016). WRF-LTNGDA: A lightning data
510 assimilation technique implemented in the WRF model for improving precipitation forecasts.
511 *Environmental Modelling and Software*, 76, 54–68.
512 Han, J., & Pan, H. L. (2006). Sensitivity of hurricane intensity forecast to convective momentum
513 transport parameterization. *Monthly Weather Review*, *134*(2), 664–674.

514 Han, J., & Pan, H. L. (2011). Revision of convection and vertical diffusion schemes in the NCEP
515 Global Forecast System. *Weather and Forecasting*, *26*(4), 520–533.
516 Hong, S. Y. (2010). A new stable boundary-layer mixing scheme and its impact on the simulated
517 East Asian summer monsoon. *Quarterly Journal of the Royal Meteorological Society*, *136*(651),
518 1481–1496.
519 Hong, S. Y., & Dudhia, J. (2012). Next-generation numerical weather prediction: Bridging
520 parameterization, explicit clouds, and large eddies. *Bulletin of the American Meteorological*
521 *Society*, *93*(1), ES6–ES9.
522 Hong, S. Y., Dudhia, J., & Chen, S. H. (2004). A revised approach to ice microphysical processes
523 for the bulk parameterization of clouds and precipitation. *Monthly Weather Review*, *132*(1), 103–
524 120.
525 Hong, S. Y., Jang, J., Shin, H. H., & Lee, J. (2012). An explicitly coupled shallow convection
526 parameterization with planetary boundary processes. Preprints. In. *12th WRF workshop*, P50.
527 Boulder, CO: NCAR.
528 Hong, S. Y., Juang, H. H., & Zhao, Q. (1998). Implementation of prognostic cloud scheme for a
529 regional spectral model. *Monthly Weather Review*, *126*(10), 2621–2639.
530 Hong, S. Y., Noh, Y., & Dudhia, J. (2006). A new vertical diffusion package with an explicit
531 treatment of entrainment processes. *Monthly Weather Review*, *134*(9), 2318–2341.
532 Hong, S. Y., & Pan, H. L. (1998). Convective trigger function for a mass-flux cumulus
533 parameterization scheme. *Monthly Weather Review*, *126*(10), 2599–2620.
534 Hong, S. Y., Park, H., Cheong, H. B., Kim, J. E. E., Koo, M. S., Jang, J., Ham, S., Hwang, S.,
535 Park, B., Chang, E., & Li, H. (2013). The global/regional integrated model system (GRIMs). *Asia-*
536 *Pacific Journal of Atmospheric Sciences*, *49*(2), 219–243.

537 Jo, E., Park, C., Son, S. W., Roh, J. W., Lee, G. W., & Lee, Y. H. (2020). Classification of localized
538 heavy rainfall events in South Korea. *Asia-Pacific Journal of Atmospheric Sciences*, *56*(1), 77–88.
539 Jung, I. W., Bae, D. H., & Kim, G. (2011). Recent trends of mean and extreme precipitation in
540 Korea. *International Journal of Climatology*, *31*(3), 359–370.
541 Kim, E. J., & Hong, S. Y. (2010). Impact of air-sea interaction on East Asian summer monsoon
542 climate in WRF. *Journal of Geophysical Research, 115*(D19), (D19).
543 Kim, Y. J., & Arakawa, A. (1995). Improvement of orographic gravity wave parameterization
544 using a mesoscale gravity wave model. *Journal of Atmospheric Sciences*, *52*(11), 1875–1902.
545 Korsholm, U. S., Petersen, C., Sass, B. H., Nielsen, N. W., Jensen, D. G., Olsen, B. T., Gill, R., &
546 Vedel, H. (2015). A new approach for assimilation of 2D radar precipitation in a high-resolution
547 NWP model. *Meteorological Applications*, *22*(1), 48–59.
548 Lagouvardos, K., Kotroni, V., Defer, E., & Bousquet, O. (2013). Study of a heavy precipitation
549 event over southern France, in the frame of HYMEX project: Observational analysis and model
550 results using assimilation of lightning. *Atmospheric Research*, 134, 45–55.
551 Lee, D. K., Kim, H. R., & Hong, S. Y. (1998). Heavy rainfall over Korea during 1980~ 1990.
552 *Korean Journal of the Atmospheric Sciences*, *1*(1), 32–50.
553 Lee, J. G., Min, K. H., Park, H., Kim, Y., Chung, C. Y., & Chang, E. C. (2020). Improvement of
554 the rapid-development thunderstorm (RDT) algorithm for use with the GK2A satellite. *Asia-*
555 *Pacific Journal of Atmospheric Sciences*, *56*(2), 307–319.
556 Lee, T. Y., & Kim, Y. H. (2007). Heavy precipitation systems over the Korean peninsula and their
557 classification. *Asia-Pacific Journal of Atmospheric Sciences*, *43*(4), 367–396.
558 Pan, H. L., & Wu, W. S. (1995). *Implementing a mass flux convection parameterization package*
559 *for the NMC medium-range forecast model*. NMC office note, pp. 40.

560 Qie, X., Zhu, R., Yuan, T., Wu, X., Li, W., & Liu, D. (2014). Application of total-lightning data
561 assimilation in a mesoscale convective system based on the WRF model. *Atmospheric Research*,
562 145, 255–266.
563 Rogers, R. F., Fritsch, J. M., & Lambert, W. C. (2000). A simple technique for using radar data in
564 the dynamic initialization of a mesoscale model. *Monthly Weather Review*, *128*(7), 2560–2574.
565 Segele, Z. T., Leslie, L. M., & Lamb, P. J. (2013). Weather Research and Forecasting Model
566 simulations of extended warm-season heavy precipitation episode over the US Southern Great
567 Plains: Data assimilation and microphysics sensitivity experiments. *Tellus A: Dynamic*
568 *Meteorology and Oceanography*, *65*(1), 19599.